SENSITIVITY OF LFC TECHNIQUES IN THE NON-LINEAR REGIME

D. M. Bushnell
NASA Langley Research Center
Hampton, Virginia

M. Y. Hussaini
ICASE, NASA Langley Research Center
Hampton, Virginia

T. A. Zang
NASA Langley Research Center
Hampton, Virginia

GROWING BOUNDARY LAYER

The boundary layer on a flat plate is illustrated in Figure 1. The streamwise, normal, and spanwise directions are denoted by x, y, and z, respectively. The displacement thickness δ^* increases in the streamwise direction. At any distance x_0 from the leading edge, one can define a Reynolds number Re based on the velocity u_∞ and kinematic viscosity ν_∞ in the free stream and the local displacement thickness.

The transition process of the growing boundary layer is influenced by significant non-linear, three-dimensional and non-parallel effects. Unfortunately, existing computer resources are only adequate for treating two out of these three effects.

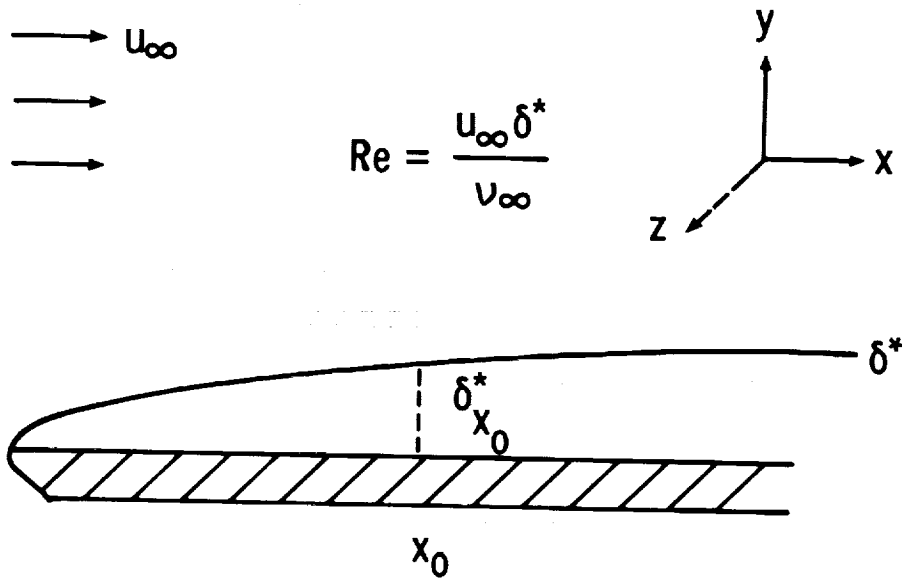

Non-linear

Three-dimensional

Non-parallel

Figure 1

PARALLEL BOUNDARY LAYER

A common compromise is to study the parallel boundary layer (see Figure 2) instead of the true, growing one. Here the focus is on the vicinity of some point x_0 (see Figure 1) and the approximation is that the displacement thickness remains constant (in x) at the value $\delta^*_{x_0}$. As a consequence, only the non-linear and the three-dimensional effects are taken into account. The neglect of the non-parallel effects should be serious only if there is appreciable growth on the scale (λ_{TS}) of the Tollmien-Schlichting (TS) waves. Since the mean flow in the parallel boundary layer is uniform in x, a Fourier approximation in x is highly accurate; moreover, only one spatial wavelength needs to be resolved for the temporal transition problem. Thus, highly resolved computations can be performed, well into the strongly non-linear regime.

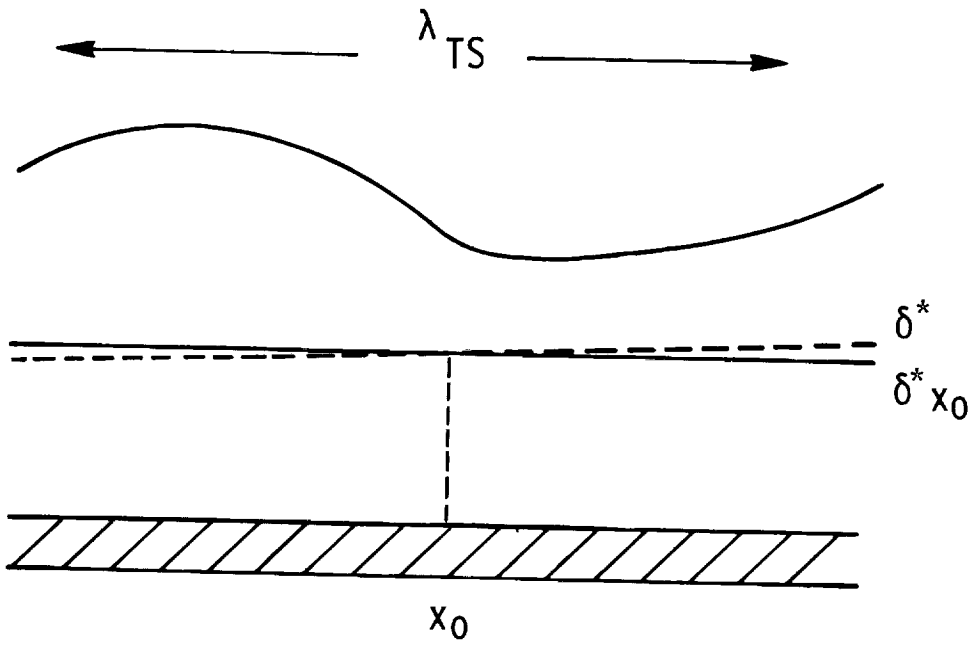

Non-linear

Three-dimensional

Figure 2

Figure 3 depicts three types of laminar-flow control (LFC) techniques. The dimensionless parameters describing self-similar solution of the Falkner-Skan boundary-layer equations are defined in the figure. These are β for pressure gradient, F_w for suction, and τ for heating. In the last case, the free stream and wall temperatures, denoted by T_∞ and T_w, respectively, (and given in degrees Kelvin), differ and the kinematic viscosity depends upon the temperature T.

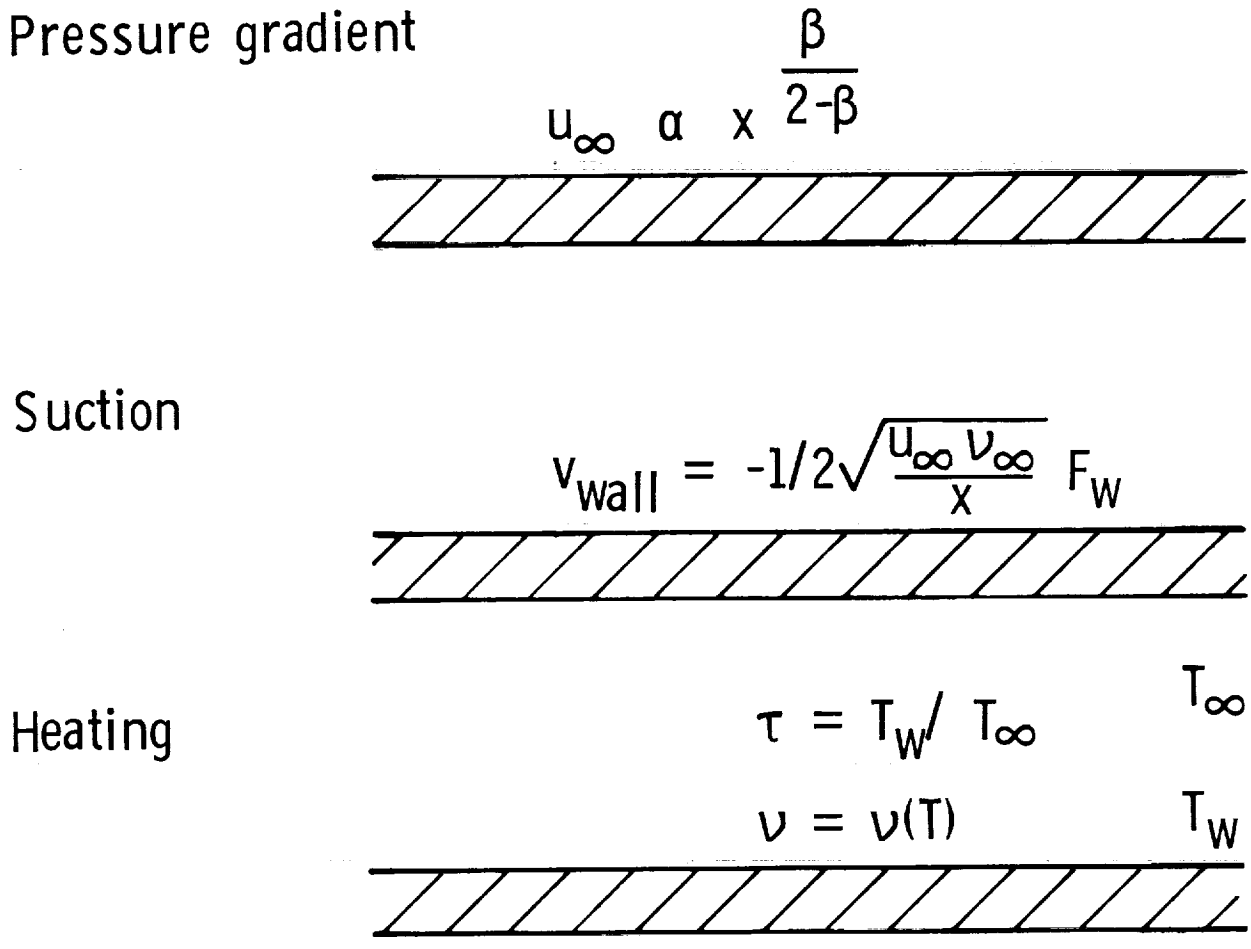

Figure 3

CONTROLLED, PARALLEL BOUNDARY LAYER

The essential features of the controlled, parallel water boundary layer are summarized in Figure 4. The mean flow is taken to be the solution of the appropriate self-similar boundary-layer equations. The temperature dependence of the viscosity and conductivity are taken from Ref. 1. (However, the specific heat and density are presumed to be independent of temperature; their values in the free stream are used throughout the flow field.) The parallel flow assumption permits the use of a periodic approximation in x and z. Shown below is the form of a single Fourier component. This alone is appropriate for the linearized stability problem, but for the full non-linear simulations reported in this paper a finite Fourier series is employed in both x and z.

- Parallel flow assumption

$$U(X, Y, Z, T) = \hat{U}(Y)\, e^{i(\alpha X + \beta Z - \omega T)}$$

- Mean flow described by Falkner-Skan equation with pressure gradient, suction and/or heating controls
- Viscosity and conductivity based on empirical formulas for water
- Reynolds numbers based on displacement thickness and free stream conditions

Figure 4

LINEAR THEORY RESULTS FOR HEATED BOUNDARY LAYERS

The linear stability of heated water boundary layers has been examined by Wazzan, Okamura, and Smith [2] and by Lowell and Reshotko [1]. Wazzan et al. included the effects of temperature only insofar as they modified the mean flow; their stability analysis admitted only velocity and pressure fluctuations. The linear results of Lowell and Reshotko, on the other hand, included the effects of temperature fluctuations. Figure 5, taken from Ref. 1, compares the neutral stability curves that ensue under heating control for $T_\infty = 60^\circ F$ when the temperature is allowed to fluctuate (solid lines) and when it is held fixed at its mean value (dashed lines). Note that the boundary layer is actually more stable than is suggested by linear theory calculations which neglect temperature fluctuations. Note also that although the flow initially becomes more stable as the wall is heated, its stability eventually degrades with additional wall heating. Lowell and Reshotko have performed further calculations in which the effects of the temperature upon the density are included. They found that this effect moves the neutral stability curves to the left, e.g., for the $T_w = 90^\circ F$ case, the solid curve moves one-third of the distance to the dashed curve when density fluctuations are admitted.

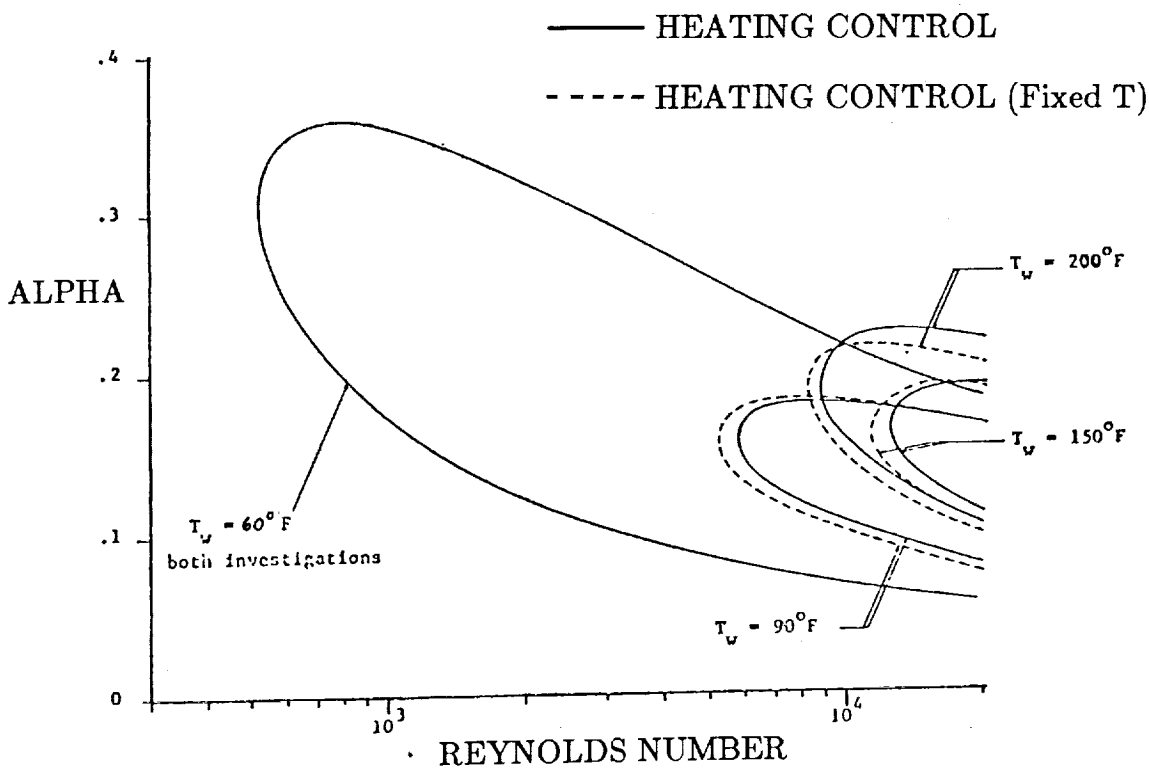

Figure 5

INCOMPRESSIBLE HEATED BOUNDARY LAYER

This paper examines LFC techniques in the non-linear regime via direct numerical solution of the time-dependent, incompressible Navier-Stokes equations, with temperature dependent viscosity and conductivity. These equations (Figure 6) are augmented with an equation for the time evolution of the temperature. In order to conform to the parallel flow assumption, forcing terms need to be added to the momentum and temperature equations. These are denoted by F_u and F_θ respectively. See Zang and Hussaini [3, 4] for more details.

$$\nabla \cdot \mathbf{u} = 0$$

$$\frac{\partial \mathbf{u}}{\partial t} + \boldsymbol{\omega} \times \mathbf{u} = -\nabla P + \frac{1}{Re}\nabla \cdot (\mu \nabla \mathbf{u}) + F\mathbf{u}$$

$$\frac{\partial \theta}{\partial t} + \mathbf{u} \cdot \nabla \theta = \frac{1}{RePr}\nabla \cdot (\kappa \nabla \theta) + F_\theta$$

$$\boldsymbol{\omega} = \nabla \times \mathbf{u}$$

$$P = p + (1/2)|\mathbf{u}|^2$$

$$\theta = (T - T_\infty)/(T_w - T_\infty)$$

Figure 6

NUMERICAL METHODS

In this work, numerical methods are needed for three problems. The mean flow is calculated from the Falkner-Skan boundary-layer equations via a fourth-order finite-difference scheme [5]. The linear eigenmodes (and linear stability properties) are computed by a Chebyshev Tau method [6]. The time dependent Navier-Stokes equations are solved by a Fourier-Chebyshev collocation method [7]. The mean flow and the linear eigenfunctions are used for the initial conditions of the direct simulation (Figure 7).

- Non-linear mean flow

  4th-order compact finite difference scheme

- Linear modes

  Chebyshev Tau method

- Navier-Stokes solution
  - Fourier-Chebyshev collocation in space
  - 3rd-order Adams-Bashforth on explicit terms
  - Crank-Nicholson on implicit terms (vertical diffusion, pressure and continuity)

Figure 7

SPLITTING METHOD

The Navier-Stokes algorithm used a splitting method which is outlined in Figure 8. The first (velocity) step accounts for the advection and diffusion terms. (Although not indicated below, the temperature equation is also integrated in this step.) The second (pressure) step enforces the incompressibility constraint. The boundary conditions in the velocity step are chosen to minimize the slip velocity which is present after the pressure step. More details are given by Zang and Hussaini [7]. The book by Canuto, Hussaini, Quarteroni, and Zang [8] contains an exhaustive discussion of spectral methods for simulations of incompressible flow.

The results reported in this paper were obtained on the NAS Cray 2. The collocation grids ranged from 16 x 48 to 64 x 64 (in x and y) for the 2-D cases and from 16 x 48 x 8 to 64 x 64 x 16 (in x, y, and z) for the 3-D problems. Typical simulations took several thousand time-steps and covered from two to five periods of the primary 2-D TS wave.

Velocity step $(t_n \rightarrow t^*)$

$$\underline{u}_t^* = \underline{u}^* \times \underline{\omega}^* + \nabla \cdot (\mu \nabla \underline{u}^*)$$

$$\underline{u}^*(\underline{x}, t_n) = \underline{u}(\underline{x}, t_n)$$

$$\underline{u}^*|_{\text{bndy}} = \underline{g}^*$$

Pressure step $(t^* \rightarrow t_{n+1})$

$$\underline{u}_t^{**} = -\nabla P^{**}$$

$$\nabla \cdot \underline{u}^{**} = 0$$

$$\underline{u}^{**}(\underline{x}, t_{n+1}) = \underline{u}(\underline{x}, t^*)$$

$$\underline{u}^{**} \cdot \hat{n} = \underline{g} \cdot \hat{n}$$

Final result $\underline{u}(\underline{x}, t_{n+1}) = \underline{u}^{**}(\underline{x}, t_{n+1})$

Figure 8

MEAN FLOW AT Re = 8950

The specific cases chosen for this investigation of non-linear stability are illustrated in Figure 9. The Reynolds number was 8950 and was chosen in part because some linear theory results were reported for this Reynolds number in Ref. 1. The free-stream temperature was 293 K. The amounts of pressure gradient, suction, and heating were chosen so that the flow was neutrally stable. (The linear theory results for the heated case did not include the temperature fluctuations.) The mean flow of both the controlled and uncontrolled cases are given in the figure. In the heated case, the viscosity varies by 50% and the conductivity by 7%. The specific heat and density (whose variations are not accounted for in the non-linear simulation) vary by 0.1% and 1%, respectively.

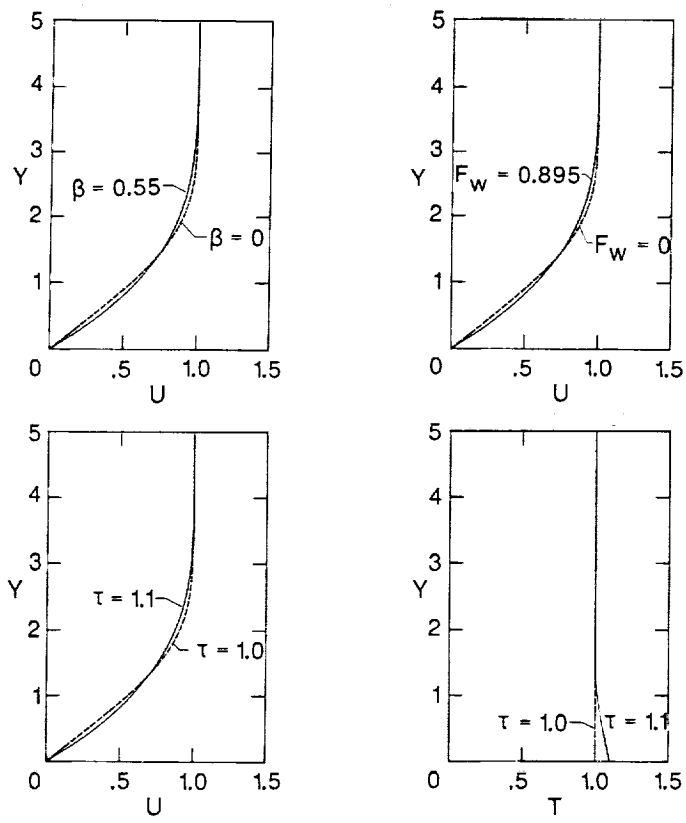

Figure 9

MEAN FLOW CHARACTERISTICS FOR Re = 8950

The use of the LFC techniques has a dramatic effect upon the actual displacement thickness of the boundary layer. This is quantified in Figure 10. The Reynolds number based on the displacement thickness of the corresponding uncontrolled boundary is also listed there. Note that in terms of the growing boundary layer, the controlled cases correspond to different positions x_0, with the pressure gradient case having the greatest distance from the leading edge and the uncontrolled case having the least distance.

CONTROL	$\delta^* / \sqrt{\frac{\nu x_0}{U_\infty}}$	Re_{δ^*} BLASIUS
NONE	1.7244	8,950
$\beta = 0.55$	0.9448	16,330
$\tau = 1.10$	1.3986	11,040

Figure 10

BOUNDARY-LAYER MODES FOR Re = 8950

The accuracy of the fully non-linear, time-dependent Navier-Stokes code is documented in Figure 11. For each of the linear modes specified in the first four columns, a highly accurate temporal eigenvalue ω and eigenfunction were generated using the Chebyshev Tau code. This eigenfunction was then input at very low amplitude into the non-linear code as the inital condition. The code was run for two TS periods and the growth rate of the eigenfunction was measured. This is listed in the last column. Listed next to it is the growth rate (imaginary part of ω) produced by the linear stability code. This growth rate is effectively zero--the real part of ω is roughly 0.04. Keeping in mind the size of the real part of ω, it is clear from Figure 11 that the non-linear code is accurate to four or five digits.

Control	Mode	α	β	Linear growth rate	Computed growth rate
Pressure	TS 2-D	0.168	0.000	0.000095	0.000096
	TS 3-D	0.168	0.168	-0.001012	-0.001028
Suction	TS 2-D	0.162	0.000	0.000093	0.000093
	TS 3-D	0.162	0.162	-0.000968	-0.000993
Heating	TS 2-D	0.150	0.000	0.000093	0.000097
	TS 3-D	0.150	0.150	-0.000798	-0.000793

Figure 11

INITIAL CONDITIONS

The initial conditions for the direct numerical simulations are depicted in Figure 12. The initial velocity field consists of the appropriate mean flow plus a 2-D TS wave and (possibly) a symmetric pair of oblique 3-D waves (only one of which is shown). The arrow denotes the streamwise direction and the indices k_x and k_z label the streamwise and spanwise Fourier components relative to the wavenumbers α and β of the 3-D TS waves given in Figure 11. The initial amplitude of the waves is measured by their maximum streamwise velocity relative to the free-stream mean flow velocity.

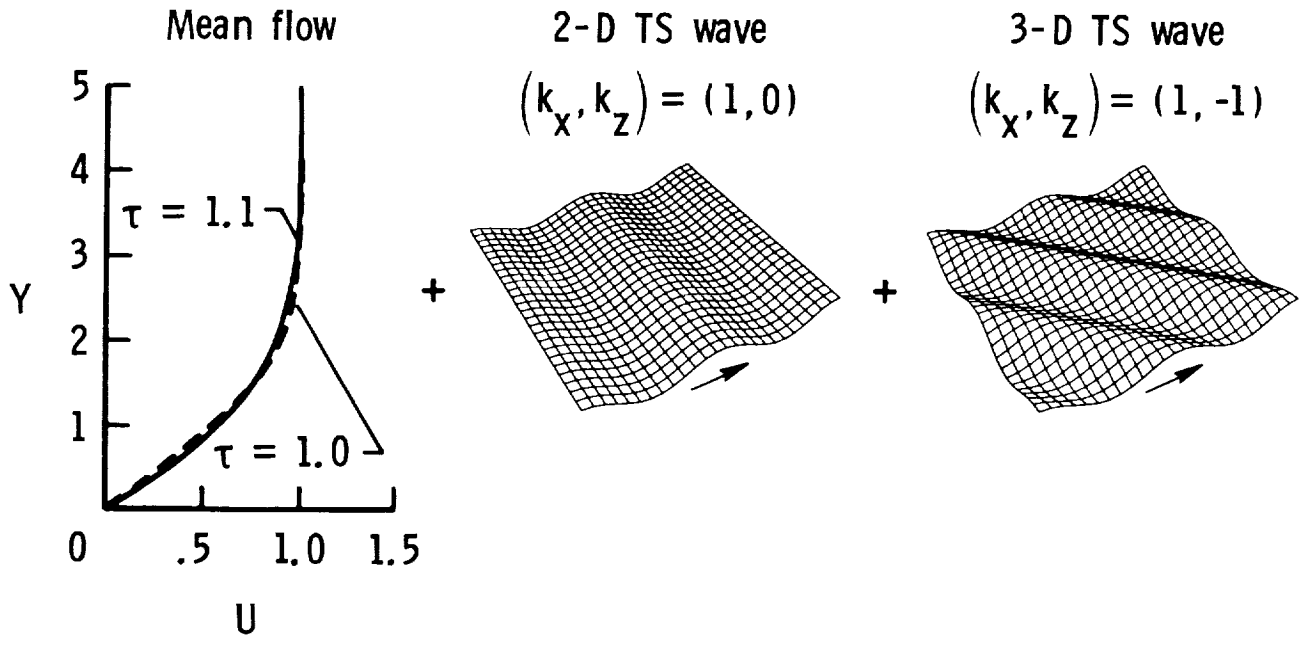

Figure 12

GROWTH OF FINITE AMPLITUDE 2-D WAVES

The first set of results pertains to finite amplitude effects upon 2-D TS waves. Results of simulations for which the initial amplitude of the 3-D wave was zero and the initial amplitude of the 2-D was 1/2, 1, 2, and 4% are summarized in Figure 13. Suction control yields behavior similar to that for pressure gradient control [4] and is therefore not given. Two types of heating control simulations were performed: in one case the temperature was held fixed at its initial mean value (corresponding to the linear theory study of Wazzan et al. [2]), and in the other the temperature fluctuations were properly accounted for (as in the work of Lowell and Reshotko [1]). The initial conditions for both types of heating simulations, however, were identical.

The strength of the perturbation at any instant is measured here by the kinetic energy E of the $(k_x,k_z) = (1,0)$ Fourier component of the velocity field. This is plotted on a semi-log scale in Figure 13, with the time measured in units of the period of the 2-D TS wave; the energy at $t = 0$ is denoted by E_0. Thus, one indication of the impact of non-linear effects is the departure of the curves from a straight (and nearly horizontal) line. Another is the failure of the curves to lie on top of each other.

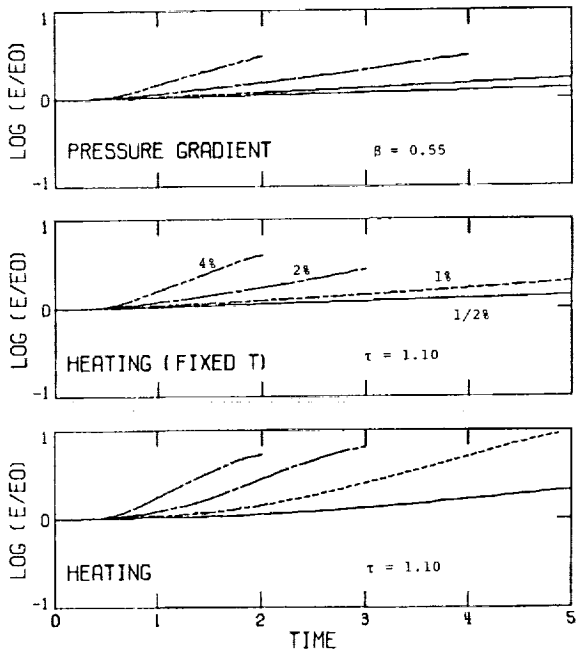

Figure 13

NON-LINEAR EFFECTS ON 2-D WAVES

In all cases, the initial growth of the 2-D TS wave is faster than exponential. Note that in the non-linear regime the heated boundary layer appears to be less stable, i.e., subjected to faster growth of the 2-D wave, when temperature fluctuations are included. This is precisely the opposite of how temperature fluctuations affect the linear stability results. It is also apparent that non-linear effects lead to a more rapid destabilization of a water boundary layer controlled by heat than one controlled by pressure gradient.

The tables below (Figure 14) summarize the departure from linear growth for 2-D waves with initial amplitudes of 1/2% and 2%. The numbers give the ratios (after 1, 2, and 3 TS periods) of the actual amplitude of the 2-D wave to that given by linear theory. These numbers, of course, just reinforce the data presented in Figure 13.

NON-LINEAR/LINEAR AMPLITUDE RATIO FOR 1/2% 2-D WAVES

TIME	PRESSURE GRADIENT	HEATING (FIXED T)	HEATING
1	1.004	1.005	1.001
2	1.013	1.017	1.016
3	1.022	1.030	1.080

NON-LINEAR/LINEAR AMPLITUDE RATIO FOR 2% 2-D WAVES

TIME	PRESSURE GRADIENT	HEATING (FIXED T)	HEATING
1	1.050	1.065	1.184
2	1.189	1.257	1.605
3	1.378	1.567	2.387

Figure 14

FUNDAMENTAL VERSUS SUBHARMONIC SECONDARY INSTABILITIES

The transition to turbulence is a strongly three-dimensional process. The next part of this investigation focuses on finite amplitude effects upon the secondary instability of the primary 2-D wave to small, 3-D perturbations. The secondary instabilities may be categorized as fundamental or subharmonic. These are identified in flow visualization of the early three-dimensional stage of transition as ordered or staggered arrays of lambda vortices [9], and have been explained by weakly nonlinear theory [10]. Figure 15 sketches the periodic array of vortices associated with these secondary instabilities. The distance L_x is the length of the primary 2-D TS wave and it is given by $2\pi/\alpha$.

The 3-D waves that lead to the fundamental instability are TS waves, i.e., solutions to the Orr-Sommerfeld equation, whereas the subharmonic instability arises from the interaction of the 2-D wave with a solution of the vertical vorticity (or Squire) equation with streamwise wavenumber $\alpha/2$. These so-called Squire modes are all linearly stable.

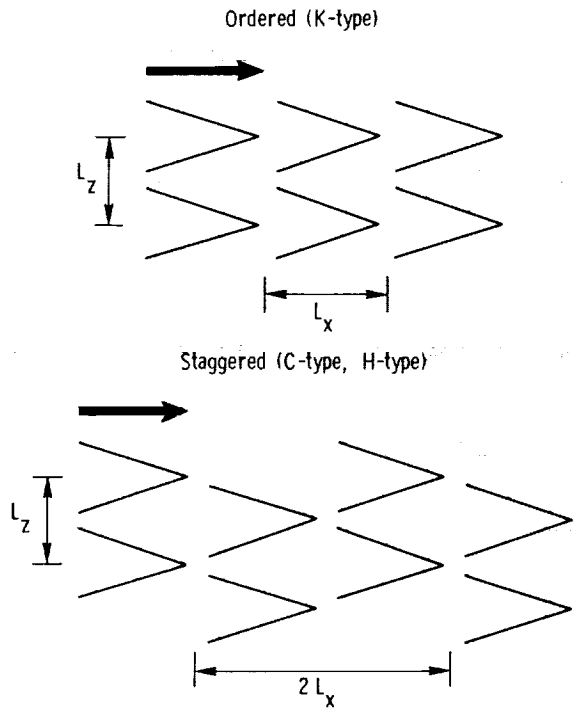

Figure 15

Figures 16, 17, and 18 summarize the results of numerical simulations of the secondary instability of controlled boundary layers. In all cases, the initial 3-D amplitude was 0.01% and the initial 2-D amplitude varied between 1/2% and 4%. In these plots, the kinetic energy is shown for the 2-D Fourier component $(k_x,k_z) = (1,0)$ and for the appropriate 3-D component--(1,1) for the fundamental instability and (1/2,1) for the subharmonic. The 3-D curves are labeled by the amplitude of the 2-D wave for the simulation.

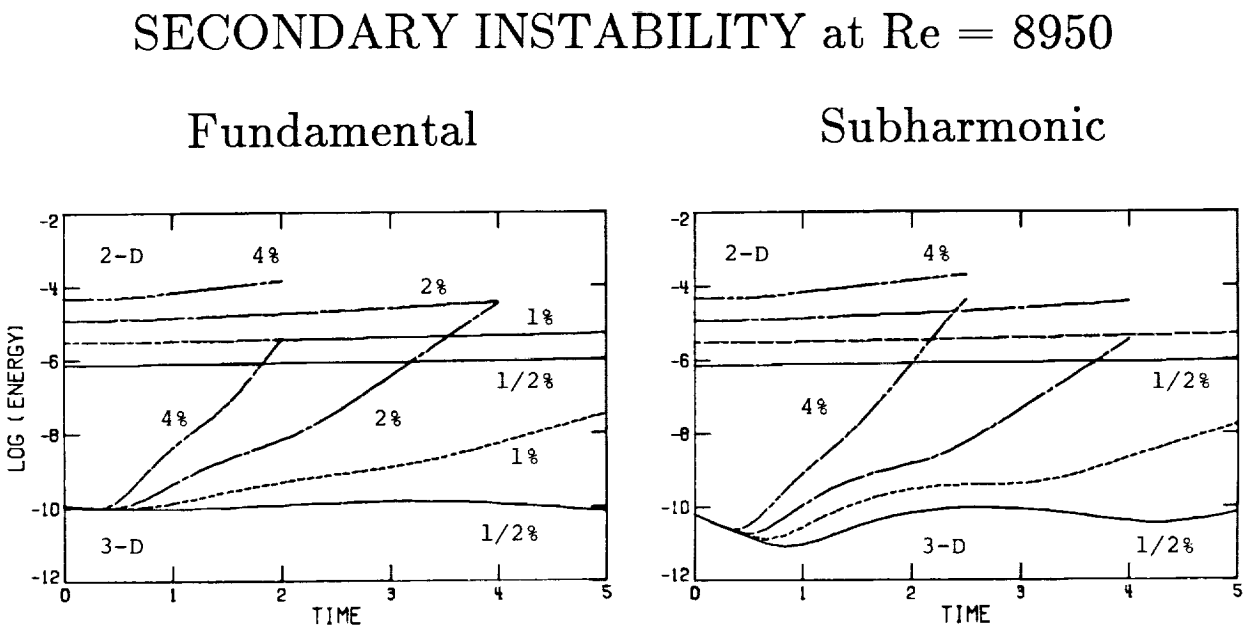

Figure 16

SECONDARY INSTABILITY FOR HEATING CONTROL (FIXED T)

The secondary instabilities have the same general character here that they do in uncontrolled boundary layers: they are triggered by 2-D amplitudes on the order of 1% or more; their growth rate increases with the 2-D amplitude; they grow much faster than the primary wave; and the fundamental and subharmonic instabilities have comparable growth rates (Figure 17).

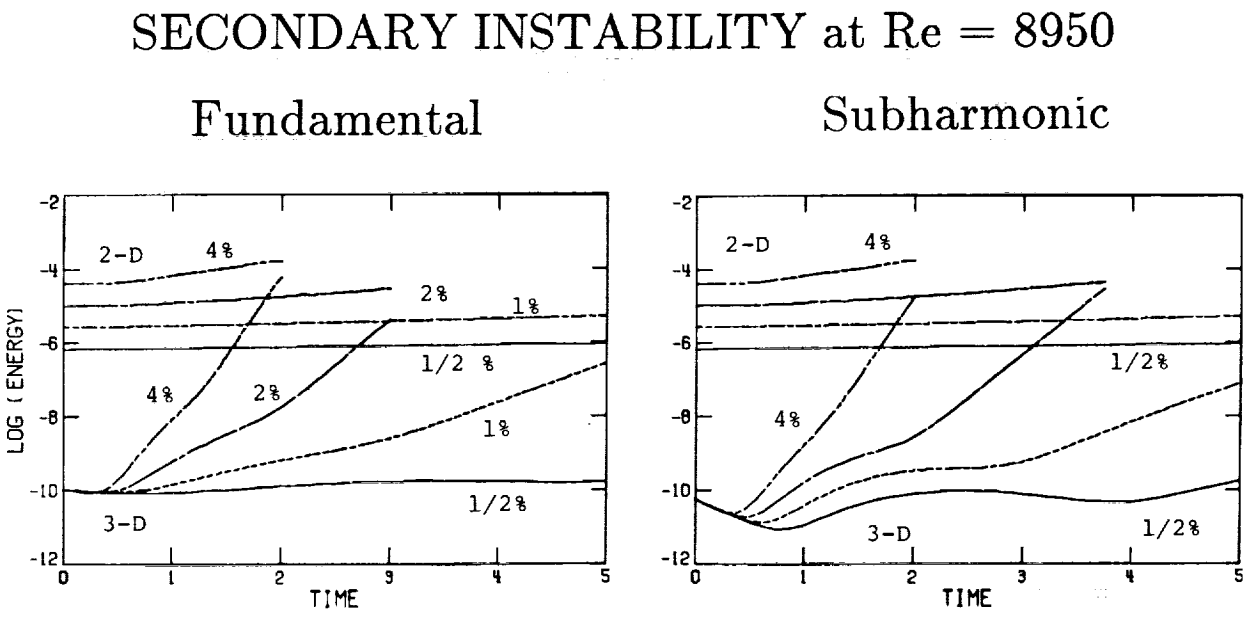

Figure 17

Among these three cases, the secondary instability is strongest for the heated boundary-layer simulation which includes temperature fluctuations. But the more rapid growth of the 3-D waves in this case is clearly tied to the more rapid growth of the 2-D wave. Hence, the principal effect of the temperature fluctuations is upon the 2-D waves (Figure 18).

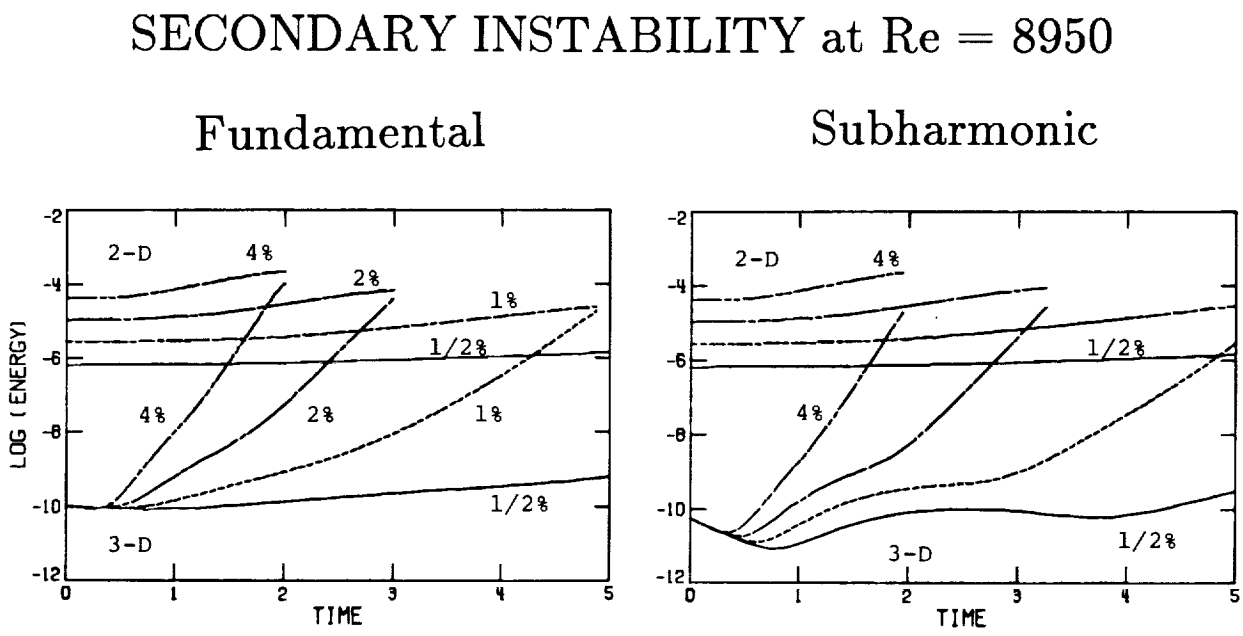

Figure 18

FLOW FIELD STRUCTURE

Figures 19 to 23, taken from the work of Zang and Hussaini [4], illustrate the flow field which develops for a fundamental (K-type) secondary instability in a heated boundary layer. The calculations were performed at a Reynolds number of 1100 and for wall heating of 2.75%. The initial amplitude was 2.7% for the 2-D wave and 0.8% for the 3-D wave. This simulation was run for nearly five periods of the 2-D TS wave; a grid of 96 x 162 x 216 (in x, y, and z) was employed in the later stages. Figures 20 - 23 display the key features at a very advanced stage of the transition process. The flat plate is indicated by the solid surface and the mean flow is from the lower right to the upper left.

The vortex lines indicate the presence of a hairpin vortex. The spanwise vorticity displays the strong detached shear layer which forms on top of the vortex. The normal velocity contours indicate the regions in which low speed fluid from the wall region is injected upward towards the free stream. The plane in the middle of the spanwise direction is known as the peak plane. It is located at the center of the hairpin vortex. In this plane, the detached shear layer is strongest and the upward normal velocity is most intense. Of special interest here are the contours of the temperature perturbation. They represent the local departure from the mean temperature. Note that the temperature fluctuations are strongly correlated with the normal velocity. There is a temperature increase in the peak plane and an even stronger temperature decrease near the wall on the outer regions of the legs of the hairpin vortex. The line drawings in figure 19 are from a slightly earlier stage and are marked with specific contour levels.

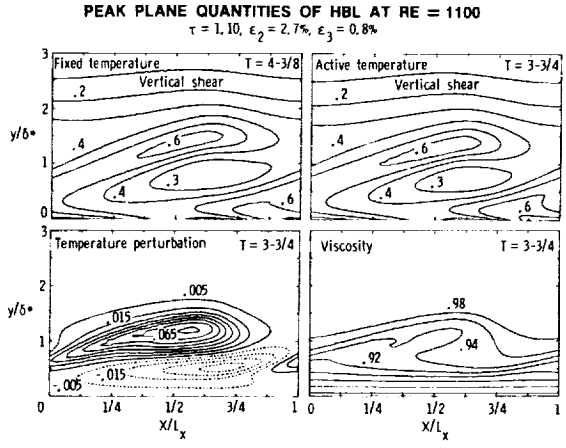

Figure 19

CONCLUSIONS

The principal conclusions from this work are summarized below. For all of the LFC techniques examined here, finite-amplitude effects are destabilizing, i.e., finite-amplitude 2-D TS waves grow faster than predicted by linear theory. We also find, in direct contrast to the results from linear theory for low-amplitude waves, that temperature fluctuations exert a further de-stabilizing influence on finite amplitude 2-D TS waves. The controlled boundary layers are, of course, subject to intense 3-D secondary instabilities. The instantaneous growth rates of both the fundamental and subharmonic instabilities are strongly tied to the amplitude of the primary 2-D wave. The principal finite-amplitude effects upon the 3-D secondary instabilities occur through the faster growth of the 2-D wave.

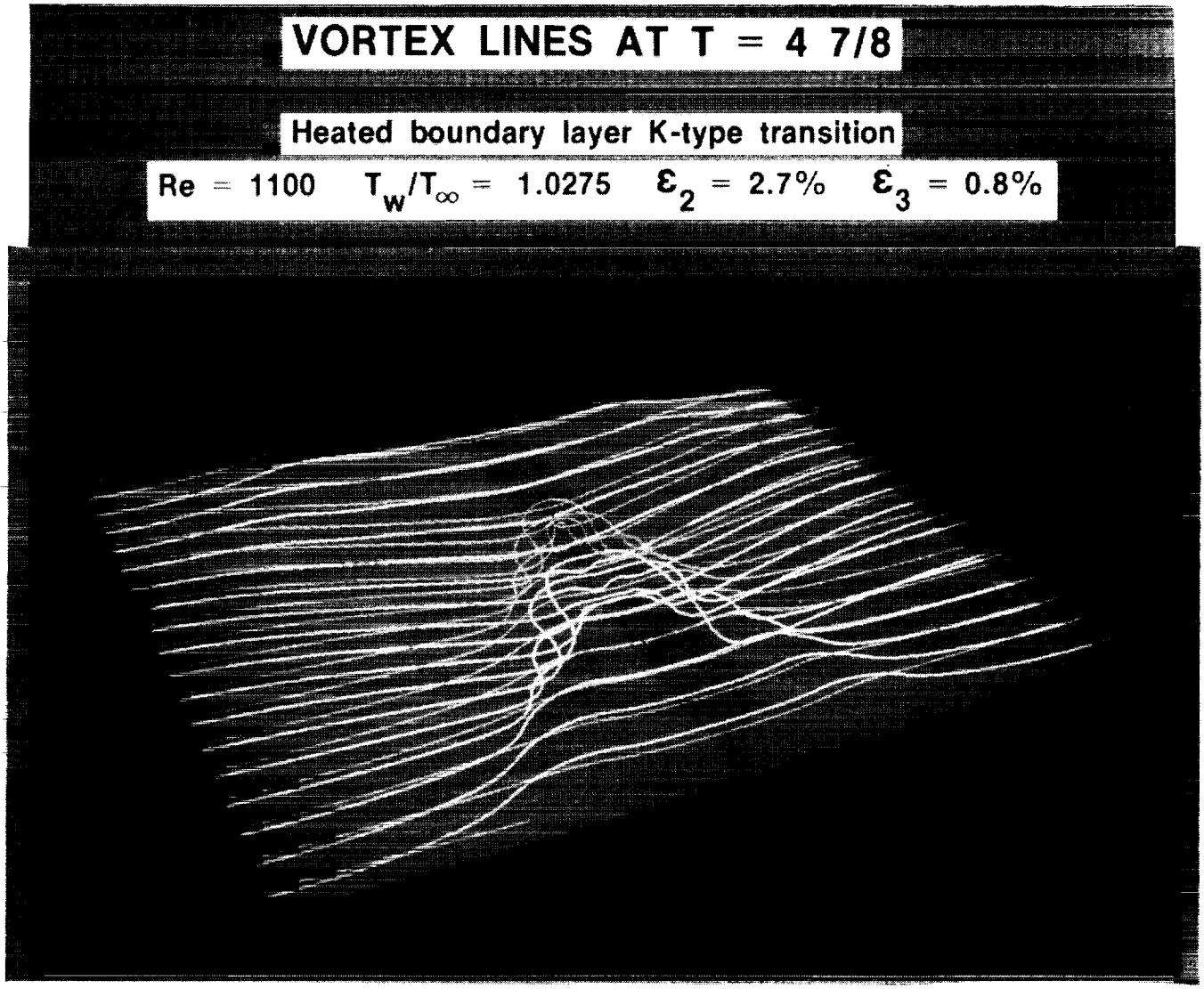

Figure 20

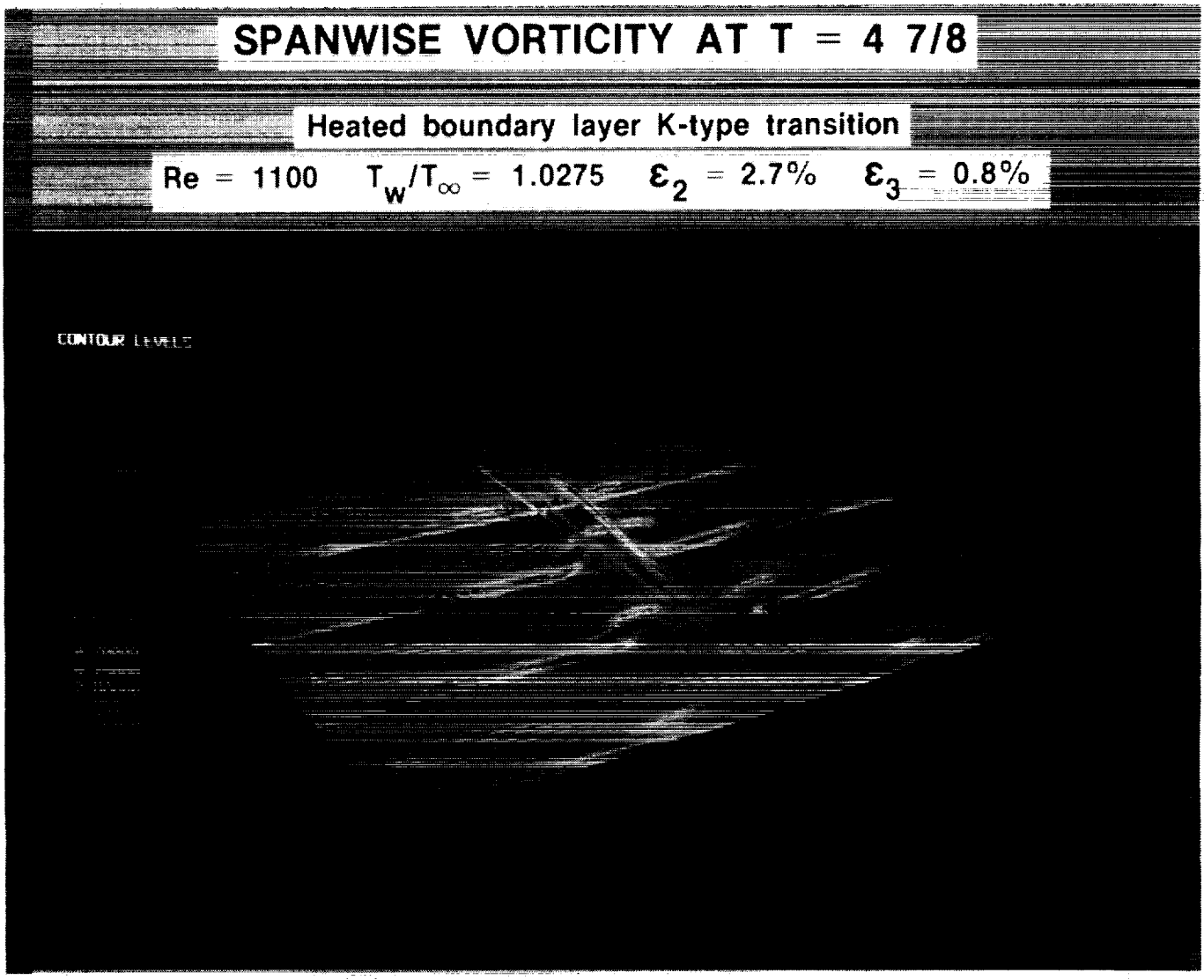

Figure 21

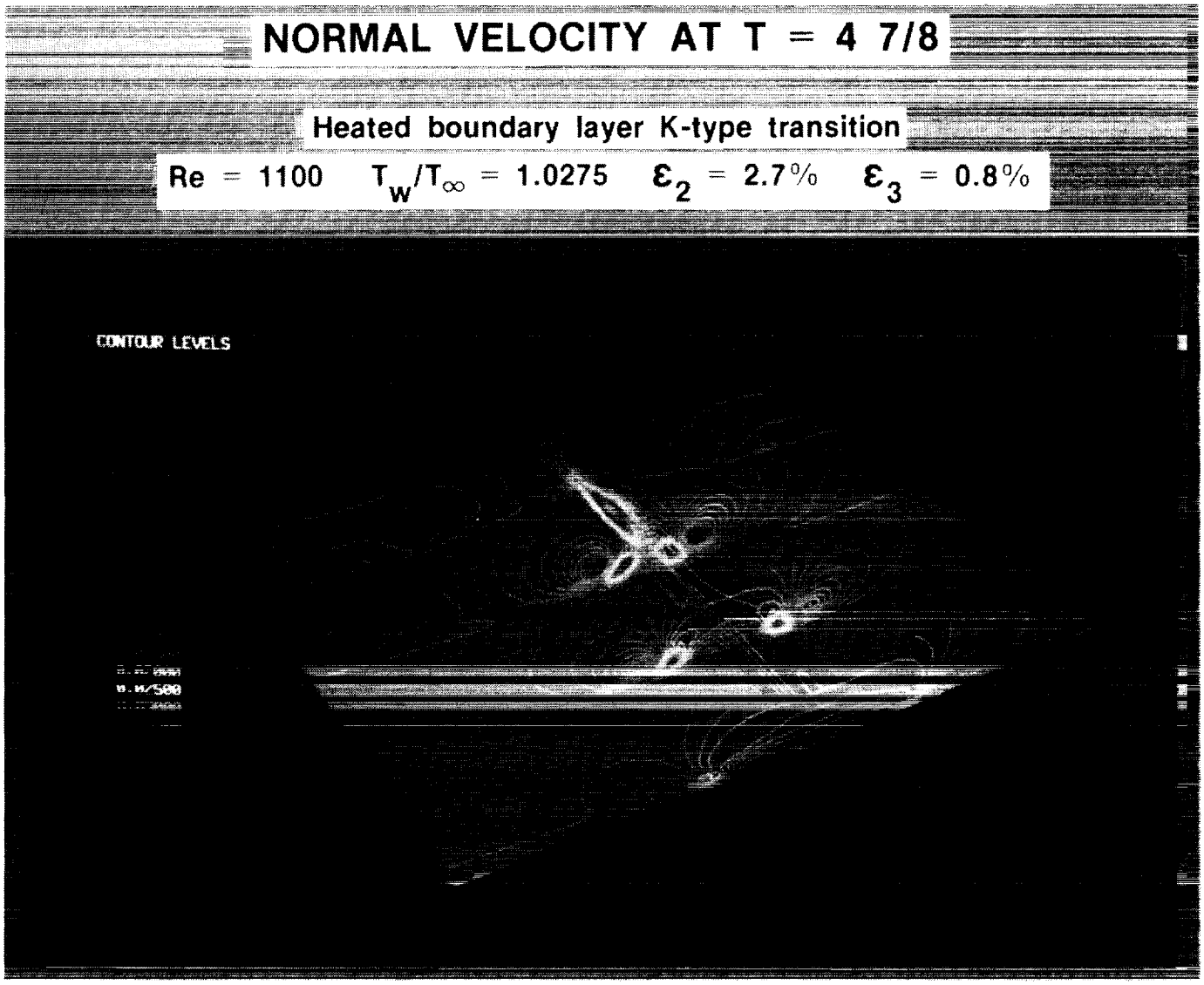

Figure 22

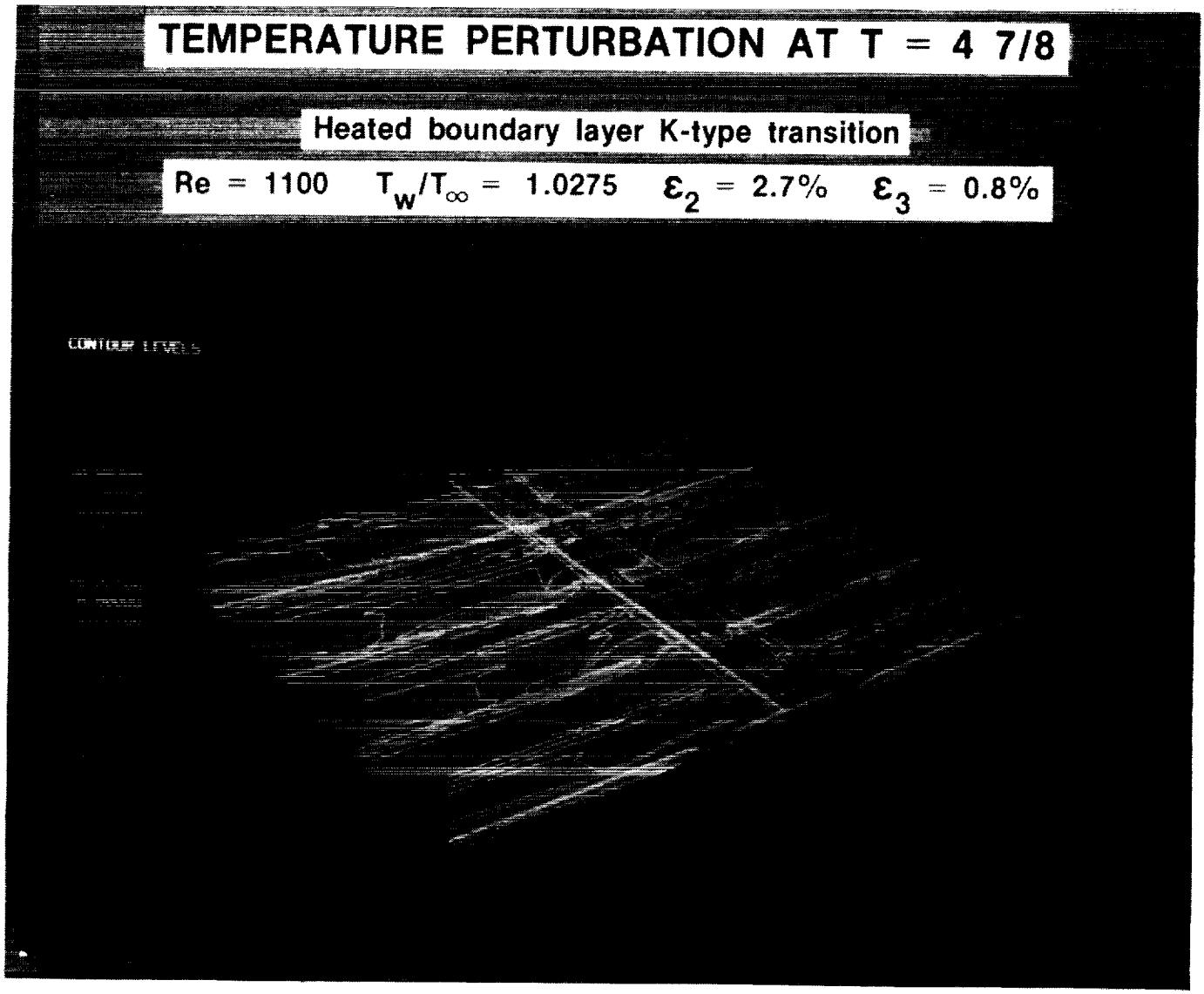

Figure 23

CONCLUSIONS

- Finite amplitude effects lead to enhanced growth of 2-D waves
- Temperature effects are further destabilizing for finite amplitude 2-D waves
- More rapid growth of the primary wave leads to more rapid development of 3-D secondary instabilities
- The fundamental and subharmonic instabilities have comparable growth rates

Figure 24

REFERENCES

1. Lowell, R. L.; and Reshotko, E.: Numerical Study of the Stability of a Heated Water Boundary Layer. Case Western Reserve University, FT AS/TR-73-93, 1974.

2. Wazzan, A. R.; Okamura, T.; and Smith, A. M. O.: The Stability of Water Flow Over Heated and Cooled Flat Plates. J. of Heat Transfer, Vol. 90, Feb. 1968, pp. 109-114.

3. Zang, T. A.; and Hussaini, M. Y.: Numerical Experiments on Subcritical Transition Mechanisms. AIAA Paper 85-0296, 1985.

4. Zang, T. A.; and Hussaini, M. Y.: Numerical Experiments on the Stability of Controlled Shear Flows. AIAA Paper No. 85-1698, 1985.

5. Malik, M. R.; Chuang, S.; and Hussaini, M. Y.: Accurate Numerical Solution of Compressible Stability Equations. ZAMP, Vol. 33, No. 2, March 1982, pp. 189-201.

6. Orszag, S. A.: Accurate Solution of the Orr-Sommerfeld Equation. J. Fl. Mech., Vol. 50, No. 4, December 1971, pp. 689-703.

7. Zang, T. A.; and Hussaini, M. Y.: On Spectral Multigrid Methods for the Time-Dependent Navier-Stokes Equations. Appl. Math. Comp., Vol. 19, pp. 359-372, 1986.

8. Canuto, C.; Hussaini, M. Y.; Quarteroni, A.; and Zang, T. A.: Spectral Methods in Fluid Dynamics. Springer-Verlag, Berlin, 1987.

9. Saric, W. S.; Kozlov, V. V.; and Levchenko, V. Y.: Forced and Unforced Subharmonic Resonance in Boundary-Layer Transition. AIAA Paper NO. 84-0007, 1984.

10. Herbert, T.: Analysis of the Subharmonic Route to Transition in Boundary Layers. AIAA Paper No. 84-0009, 1984.